remote sensing

MDPI

Article

Initial Tropospheric Wind Observations by Sanya Incoherent Scatter Radar

Ning Zhang [1,2], Xinan Yue [1,2,3,*], Feng Ding [1,2,3], Baiqi Ning [1,2], Junyi Wang [1,2,3], Junhao Luo [1,2], Yonghui Wang [1,2,3], Mingyuan Li [1,2,3] and Yihui Cai [1,2,3]

[1] Key Laboratory of Earth and Planetary Physics, Institute of Geology and Geophysics, Chinese Academy of Sciences, Beijing 100029, China; zhangn@mail.iggcas.ac.cn (N.Z.); dingf@mail.iggcas.ac.cn (F.D.); nbq@mail.iggcas.ac.cn (B.N.); wangjunyi@mail.iggcas.ac.cn (J.W.); luojunhao@mail.iggcas.ac.cn (J.L.); wangyonghui19@mails.ucas.ac.cn (Y.W.); limingyuan@mail.iggcas.ac.cn (M.L.); caiyihui@mail.iggcas.ac.cn (Y.C.)

[2] Beijing National Observatory of Space Environment, Institute of Geology and Geophysics, Chinese Academy of Sciences, Beijing 100029, China

[3] College of Earth and Planetary Sciences, University of Chinese Academy of Sciences, Beijing 100049, China

* Correspondence: yuexinan@mail.iggcas.ac.cn

Abstract: Sanya incoherent scatter radar (SYISR) is a newly developed phased array incoherent scatter radar in the low latitudes of China located at Sanya (18.3°N, 109.6°E), Hainan Province. The main objective of SYISR is to observe the ionosphere. Given its frequency and power, it should have the capability to observe the troposphere. In this study, we show several tropospheric wind experiments that may indicate radar function expansion and capability verification, although observing the troposphere will not be an operation mode in the future. Reliable radar echoes were detected by SYISR up to 20 km with a turbulence scale of 0.35 m and a frequency of 430 MHz. Generally, both the geometric (GEO) method and the velocity azimuth display (VAD) method give similar wind profiles. Above 10 km, the discrepancy between the two methods becomes nonnegligible. For the same method, the discrepancy above 15–20 km among winds derived from different zenith angle measurements is nonnegligible. The VAD methods give more reasonable results at higher altitudes. The standard deviation of the difference (SYISR radar minus the reanalysis data ERA5) for zonal wind and meridional wind was 1.1 m/s and 0.78 m/s, respectively. During rainfall, we can distinguish the spectrum of rainfall and atmospheric turbulence from the power spectrum according to the spectral widths and Doppler frequency shifts.

Keywords: tropospheric wind; atmospheric turbulence; SYISR; multibeam measurement

check for updates

Citation: Zhang, N.; Yue, X.; Ding, F.; Ning, B.; Wang, J.; Luo, J.; Wang, Y.; Li, M.; Cai, Y. Initial Tropospheric Wind Observations by Sanya Incoherent Scatter Radar. *Remote Sens.* **2022**, *14*, 3138. https://doi.org/10.3390/rs14133138

Academic Editor: Michael E. Gorbunov

Received: 7 June 2022
Accepted: 24 June 2022
Published: 29 June 2022

Publisher's Note: MDPI stays neutral with regard to jurisdictional claims in published maps and institutional affiliations.

Copyright: © 2022 by the authors. Licensee MDPI, Basel, Switzerland. This article is an open access article distributed under the terms and conditions of the Creative Commons Attribution (CC BY) license (https://creativecommons.org/licenses/by/4.0/).

1. Introduction

The Earth's atmosphere is the layer of mixed gases that surrounds the earth. According to the changing characteristics of atmospheric temperature, from low to high altitudes, the atmosphere is divided into the troposphere, stratosphere, mesosphere, thermosphere, and the escape layer. The lower atmosphere includes the troposphere, which is most closely related to human activities. Strictly speaking, it refers to the area of the Earth's atmosphere from 0 to below 25 km above sea level [1]. It is the main area of weather changes and occupies more than 80% of the air quantity. Frequent violent convective movement and a large amount of water vapor impurities in the layer lead to clouds, rain, snow, and other weather phenomena. The troposphere is also the main source area of atmospheric fluctuations. Intense atmospheric activities can in turn lead to the excitation of convective gravity waves [2]. Therefore, it is very important to monitor the troposphere for studies of atmospheric circulation and climate change.

At the beginning of the twentieth century, with the development of radio technology, some advanced countries began to develop radiosondes to detect troposphere and

lower stratosphere horizontal wind. In 1936, Colwell et al. [3] and Watt et al. [4] detected atmospheric echoes from a level below 5 km using zenith radio waves with wavelengths of ~5 m in the United States and the United Kingdom, respectively. In the 1940s, many meteorological remote sensing devices were applied to atmospheric detection. In the troposphere, the random nonuniform distribution of the refractive index caused by turbulent motion is the main mechanism for the generation of radar echoes in this region [5]. In the tropopause and stratosphere, due to the existence of reverse humidity, there is a strong vertical uneven distribution of the refractive index. This vertical distribution structure can produce a Fresnel reflection phenomenon for vertically incident electromagnetic waves [6].

Radar technology, such as wind profiler radar and MST (mesosphere stratosphere and troposphere) radar, is a very powerful tool for remotely sensing the Earth's atmosphere. Wind profiler radar can continuously provide the distribution of meteorological elements such as the atmospheric horizontal wind field, vertical wind field, and atmospheric refractive index structure constant with height [7]. The transmission power of wind profiler radar is usually at the kilowatt level, so the detection height of wind profiler radar is generally a few kilometers to more than ten kilometers. For the troposphere and stratosphere, MST radar is usually used in the very high-frequency (VHF) band [8]. In addition to observing the troposphere and stratosphere, MST radar, such as the Jicamarca radar in Peru, can also observe the thermal scattering of electrons in the mesosphere or the scattering echoes of electron clusters of a certain scale [9–12]. Jicamarca radar operates in a VHF band of 49.92 MHz and is capable of acquiring echoes in the troposphere, stratosphere, and mesosphere. However, the range resolution of Jicamarca radar is only 3000 m [13], which does not allow for finer wind field detection. The working frequency of middle and upper atmosphere (MU) radar is 46.5 MHz, and the peak transmission power can reach 1 megawatt (MW). A circular antenna array composed of 475 Yagi antennas can realize beam scanning in five directions [14–16]. SOUnding System (SOUSY) radar is a series of radar networks, and the first one is SOUSY Harz radar. After decades of development, the most representative one is SOUSY Svalbard radar for polar atmospheric observation research [17]. Its working frequency is 53.5 MHz and its peak power is 70 kW. It consists of 356 four-element Yagi antennas, the beam inclination angle is 5 degrees, and the inclined beams are northeast, southeast, southwest, and northwest. With the funding of the National Major Scientific Project Meridian Chain Project (referred to as the Meridian Project), China has built two MST radar stations in Wuhan and Beijing. The frequencies of the Wuhan and Beijing MST radar stations are 53.8 MHz and 50 MHz, respectively. The antenna arrays of the Beijing and Wuhan MST radar systems are composed of 576 three-element linearly polarized Yagi antennas arranged in an equidistant 24 $\times$ 24 square matrix. The peak power is 172.8 kW, and the beam width is 3.2° [18–21]. The Arecibo radar station, built as an incoherent scatter radar in Puerto Rico, was also used to observe wind [22–27]. The Arecibo radar operated in the ultrahigh-frequency (UHF) band of 430 MHz and is similar to the wind profiler radar system. It can be used to observe the wind field in the troposphere, and its best height resolution is 150 m. Arecibo radar can obtain echoes at 30 km due to its advantages of high power and large aperture, but the time resolution is poor due to its mechanical rotation.

In Sanya (18.3°N, 109.6°E), a low latitude station in China, a phased array incoherent scatter radar (SYISR) was recently built. It transmits right-handed circularly polarized electromagnetic waves and receives left-handed circularly polarized echoes [28]. It consists of 128 subarrays, with a transmit peak power of 2 MW and an adjustable operating frequency band of 430–450 MHz, making it similar to the tropospheric wind profiler radar. SYISR uses the newest radar technologies, including an active digital phased array and all solid-state transmitting and digital receiving. It can switch beam pointing in milliseconds (ms) and set up any arbitrary beam as needed in the radar effective detection area, so it is suitable for tropospheric wind detection in a flexible way. To address the risk of large arrays during the construction of the SYISR, a preliminary tropospheric wind field experiment was carried out with eight subarrays (SYISR-8) [29] to obtain tropospheric wind field information, but

the effective detection height was less than 10 km. The consistency was evaluated first by comparing the wind results with SYISR-8, dedicated balloon-based global positioning system (GPS), and co-located radiosonde results. They showed similar altitude variations, indicating that the SYISR-8 could be used for wind profiling with reliable accuracy.

In this paper, we show the wind experiments performed by SYISR. In comparison with previous experiments using ISR for wind derivation, our radar has a more flexible beam configuration given its digital phase screening characteristic. This experiment can, on the one hand, expand the function of SYISR and, on the other hand, validate the capability of radar from a different perspective than ionospheric experiments. Note that the main objective of SYISR is ionosphere monitoring, and tropospheric observation experiments will not be a daily operational mode in the future.

2. Methods

To obtain three-dimensional wind field information, at least three noncoplanar beams are needed. Wind profiler radar and MST radar generally use five beams for wind field observations [7,18]. Given the fast beam switching and flexible beam pointing, we can actually set up many more than five beams at different elevations and azimuths as needed. We performed tropospheric wind experiments during three different time intervals during 17–21 July 2021, with different beam configurations (Table 1). The waveform used was a long pulse with a 2 μs pulse width, corresponding to a range resolution of ~300 m. The radar frequency used was 430 MHz. Three beam numbers, 9, 25, and 41, were tested. In all the experiments, radar sampled the echoes in the range of 1.8–45 km. As an illustration, a schematic of the configuration of 25 beams and 41 beams is shown in Figure 1. For the 25-beam experiment, as shown in Figure 1a, one beam had a zenith angle of 0°, the other tilt beam corresponded to a zenith angle of 15°, and the azimuth angle ranged from 0° to 345°, with an interval of 15°. For the 41-beam experiment, as shown in Figure 1b, one beam had a zenith angle of 0°, and the remaining 40 beams corresponded to zenith angles of 3°, 6°, 9°, 12°, and 15°. The corresponding azimuth angles were 0°, 45°, 90°, 135°, 180°, 225°, 270°, and 315°. For the 9-beam experiment (not shown in Figure 1), one beam pointed in the zenith direction, and the other eight beams had a zenith angle of 15°, with azimuths of 0°, 45°, 90°, 135°, 180°, 225°, 270°, and 315°. In the experiment, the radar beam stayed for 30 s in each direction, and one integral detection cycle completed scans in all beam directions.

Table 1. Experimental time interval.17 July 2021.

#	Pulse Mode	Beam Number	Starting Time	End Time	Start Gate (km)	End Gate (km)
1	Long pulse	9	17 July 2021 08:50	18 July 2021 08:50	1.8	45
2	Long pulse	25	18 July 2021 18:30	19 July 2021 09:00	1.8	45
3	Long pulse	41	21 July 2021 13:45	21 July 2021 22:00	1.8	45

In this study, we adopted the classic processing method of wind profile radar [18]. After averaging the echo signal in the time domain, removing the direct current (DC), fast Fourier transform (FFT) spectrum analysis, spectral averaging, noise reduction, removing ground clutter, and other steps, we obtained the power spectral density [30–33]. Based on the power spectral density data, the echo signal was identified, and the spectral moment was extracted to obtain the echo power intensity, radial velocity, spectral width, and other information. Then, assuming the consistency and continuity of the stable airflow, erratic data points were removed. Finally, the radial velocities were derived. Table 2 summarizes the main signal processing parameters used in the study.

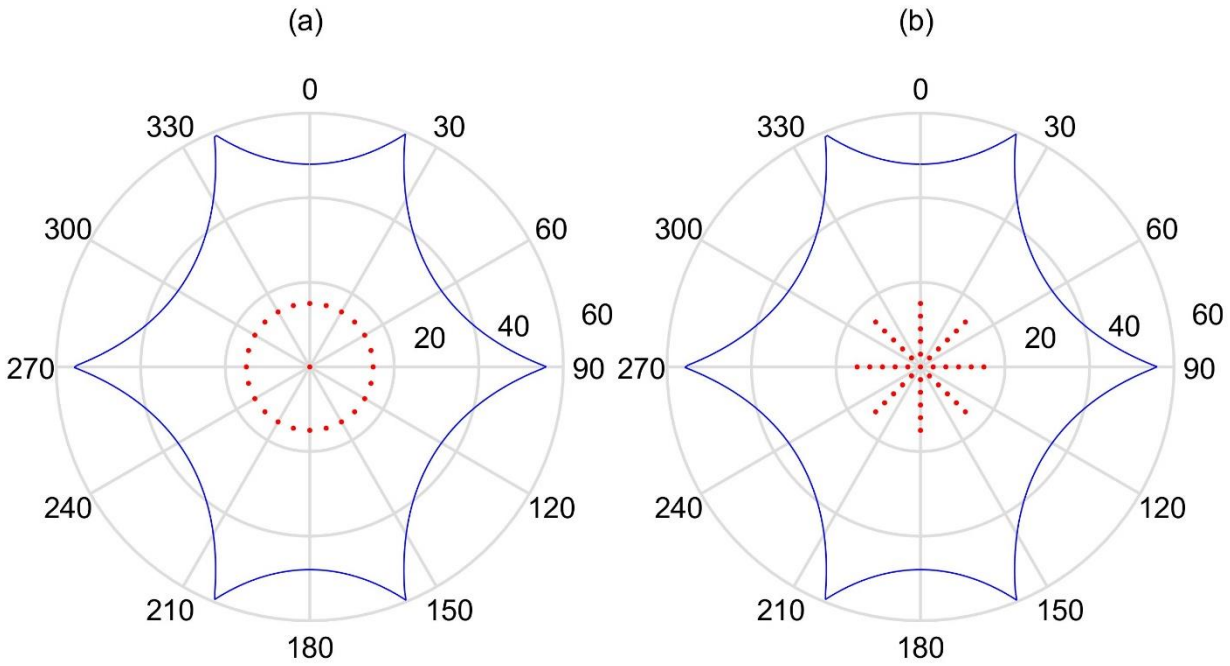

Figure 1. (**a**) Schematic of 25 beams and (**b**) schematic of 41 beams.

Table 2. Signal processing parameter configuration.

Coherent integration times	16	**FFT points**	256
Spectral average times	7	**Sampling frequency (MHz)**	4
Receive bandwidth (MHz)	4	**Beam dwell time (s)**	30
Transmitting pulse width (μs)	2	**Interpulse period (μs)**	1000

Using radial velocity to detect horizontal wind requires certain assumptions about the distribution of the horizontal wind field. One method uses the assumption of a horizontally uniform wind field. This method mainly calculates the horizontal wind field through a geometric (GEO) method. This method generally uses three beams to obtain the horizontal wind field. However, because the vertical velocity is relatively small, the vertical velocity error of the vertical beam measurement is large. In practice, five beams are used more frequently [18].

Assuming a uniform wind field, we can derive the horizontal wind velocity from the radial velocity obtained by the spatially scanned beams [32,34]. The formula is as follows:

$$\begin{cases} u = (V_{re} - V_{rz}cos\theta)/sin\theta \\ v = (V_{rn} - V_{rz}cos\theta)/sin\theta \end{cases} \quad (1)$$

where V_{re} is the radial velocity in the east direction, V_{rn} is the radial velocity in the north direction, and V_{rz} is the radial velocity in the zenith direction. θ is the zenith angle corresponding to the tilt beam.

Another method of calculating the horizontal wind field is based on the linear wind field assumption. In the tropopause or stratosphere area, especially in areas with strong turbulence, the assumption of a linear wind field is closer to the real situation of the atmospheric wind field. When using the linear wind field assumption, the so-called velocity azimuth display (VAD) algorithm is usually used [35–38]. During scanning, the radial velocity on the same elevation circle can be used to estimate the horizontal winds.

The velocity components V_x and V_y may be expressed in terms of their value at the center of the scanned circle (subscript 0) and mean linear velocity terms, as follows:

$$\begin{cases} V_x = V_{x0} + \overline{\frac{\partial V_x}{\partial x}} x + \overline{\frac{\partial V_x}{\partial y}} y \\ V_y = V_{y0} + \overline{\frac{\partial V_y}{\partial x}} x + \overline{\frac{\partial V_y}{\partial y}} y \end{cases} \quad (2)$$

where $x = rcos\beta$, $y = rsin\beta$, and r is the horizontal range. In the analysis, the horizontal change in the vertical wind can be ignored. The radial velocity is expressed as

$$\begin{aligned} V_R(\beta) = \tfrac{1}{2} rsin\theta \quad & \left(\overline{\frac{\partial V_x}{\partial x}} + \overline{\frac{\partial V_y}{\partial y}} \right) + V_{f0} cos\theta - V_{x0} sin\theta cos\beta - V_{y0} sin\theta sin\beta \\ & - \tfrac{1}{2} risn\theta \left(\overline{\frac{\partial V_x}{\partial x}} - \overline{\frac{\partial V_y}{\partial y}} \right) cos2\beta - \tfrac{1}{2} rsin\theta \left(\overline{\frac{\partial V_x}{\partial y}} + \overline{\frac{\partial V_y}{\partial x}} \right) sin2\beta \end{aligned} \quad (3)$$

where θ represents the zenith angle of the tilt beam and β represents the azimuth of the beam. V_R is positive toward radar, and V_{f0} is positive downward.

The horizontal wind velocity is expressed as

$$V_h = -\left(\left(\frac{2}{M} \sum_{i=1}^{M} V_{Ri} cos\beta_i \right)^2 + \left(\frac{2}{M} \sum_{i=1}^{M} V_{Ri} sin\beta_i \right)^2 \right)^{\frac{1}{2}} / sin\theta \quad (4)$$

where M represents the number of beams with different azimuths.

3. Results and Discussion

3.1. Radial Velocity

When using SYISR for multibeam detection, a pulse is sent in different beam directions and a back-reflection signal is received within a detection cycle. Because the atmospheric turbulence echo is a random signal mixed with various clutter, the intensity is very weak, the pulsation is strong, and the spectrum is very wide. Therefore, data processing is needed. The I/Q signal contains the amplitude and phase information of the atmospheric echo signal.

Figure 2 shows an observational example of the power spectral Doppler frequency shift of eight tilt beams in the 9-beam experiment at 10:00 on 17 July 2021. To clearly show the Doppler frequency shift, we used dB as the unit of the echo power spectra. As shown in Figure 2, the effective echo power was obtained up to 20 km. The detection height increased by more than 10 km compared with that of the previous prototype SYISR-8. The main reason was that the radar transmitting power was much larger than that of SYISR-8. As the transmitting power increased, the corresponding detection capability increased. However, the effective detection height of radar was not only determined by detection power but also related to the transmitting frequency. Turbulence exists at different heights, but the intensity and scale of turbulence are different for different heights [39,40]. In the Arecibo observational experiment [27], the observable highest height varied from 20 km to 30 km, while that of SYISR was approximately 20 km. One important reason is that the power aperture product of Arecibo is much larger than that of SYISR, which may make the highest detectable height of Arecibo higher.

Figure 3 shows that, the Doppler shift of the two symmetrical azimuth beams had good symmetry, indicating good radar observations. The Doppler frequency shift above 10 km gradually increased in some directions. As shown in Figure 3d, the Doppler radial velocity in the southeast direction (Figure 3d) reached 3.6 m/s at 10:00 on 17 July 2021. Figure 3 also shows that the echo signal strength was relatively large below 10 km, while it became weak above 10 km, and the noise signal gradually became obvious.

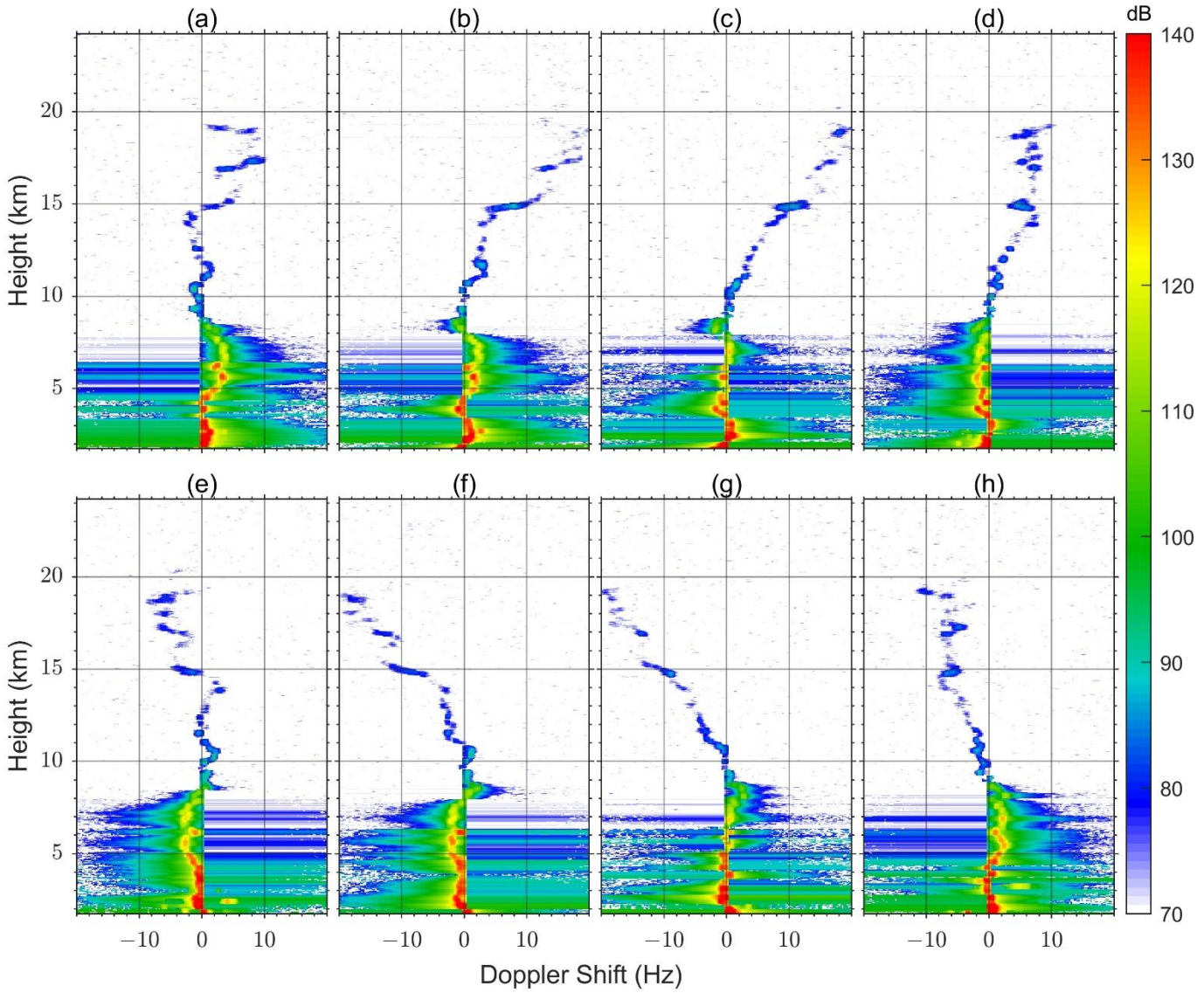

Figure 2. Echo power spectrum corresponding to the eight azimuths of 0° ((**a**) north), 45° ((**b**) northeast), 90° ((**c**) east), 135° ((**d**) southeast), 180° ((**e**) south), 225° ((**f**) southwest), 270° ((**g**) west), and 315° ((**h**) northwest) with a zenith angle of 15°. The unit is dB, and the experiment time was 10:00 local time on 17 July 2021.

As a first step, we focused on the signal-to-noise ratio (SNR) variations versus height, zenith angle, and azimuth, as shown in Figure 4. The SNR generally decreased with increasing height, regardless of the zenith angle and azimuth. However, there was some abnormal enhancement, which was probably related to the enhanced turbulence activities. The SNR gradually decreased as the zenith angle increased, due to the corresponding variations in radar gain. For the azimuth distribution, the SNR was asymmetric for the geographically symmetric beams. However, the SNR was obviously larger in the south–north direction than that in the east–west direction, due to the beam width differences.

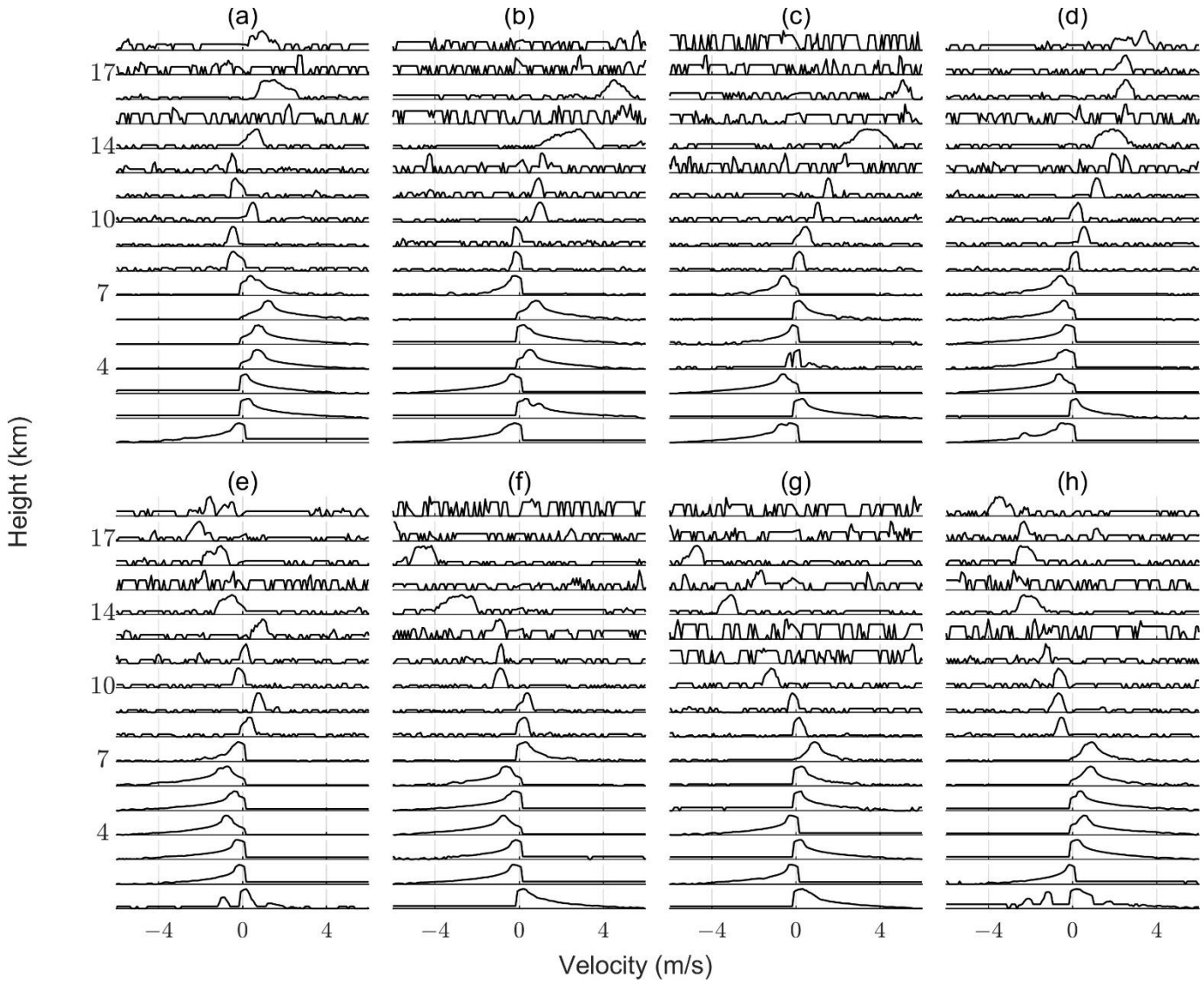

Figure 3. Derived Doppler velocity for the selected heights corresponding to Figure 2. ((**a**) north), 45° ((**b**) northeast), 90° ((**c**) east), 135° ((**d**) southeast), 180° ((**e**) south), 225° ((**f**) southwest), 270° ((**g**) west), and 315° ((**h**) northwest) with a zenith angle of 15°. The unit is m/s, and the experiment time was 10:00 local time on 17 July 2021.

3.2. Horizontal Wind Velocity

To evaluate and analyze the horizontal wind velocities calculated by the VAD and GEO methods, we used the data of 25 beams to calculate the horizontal velocities from 18:30 on 18 July 2021 to 09:00 on 19 July 2021, in experiment #2. The average horizontal winds and standard deviation were calculated in this period, as shown in Figure 5. The maximum zonal wind velocity was close to 12 m/s for the VAD and GEO methods, while the maximum meridional wind velocity was close to 5 m/s for the VAD method and 6 m/s for the GEO method. The zonal wind reached its maximum at 13 km for the VAD and GEO methods, and the meridional wind reached its maximum at 17 km for the VAD method and 18 km for the GEO method. The zonal and meridional winds obtained by the two methods below 10 km were almost the same. Above 10 km, the zonal and meridional winds obtained by the two methods were different. The standard deviations of the zonal and meridional winds calculated by the VAD method were smaller and varied insignificantly with height. The standard deviations of the GEO method roughly increased with height. The maximum standard deviations of the zonal winds obtained by the GEO and VAD

methods were 4.79 m/s at approximately 14 km and 2.81 m/s at approximately 17 km, but were 3.12 m/s and 2.55 m/s at a same height of 17 km for the meridional wind. In general, the standard deviations of the VAD method at all altitudes were smaller than those of the GEO method. Due to the difference between the fitting method of VAD and the decomposition method of GEO, the horizontal wind obtained by the VAD method was more stable when using 24-beam (except zenith angle 0°) data to solve the horizontal wind.

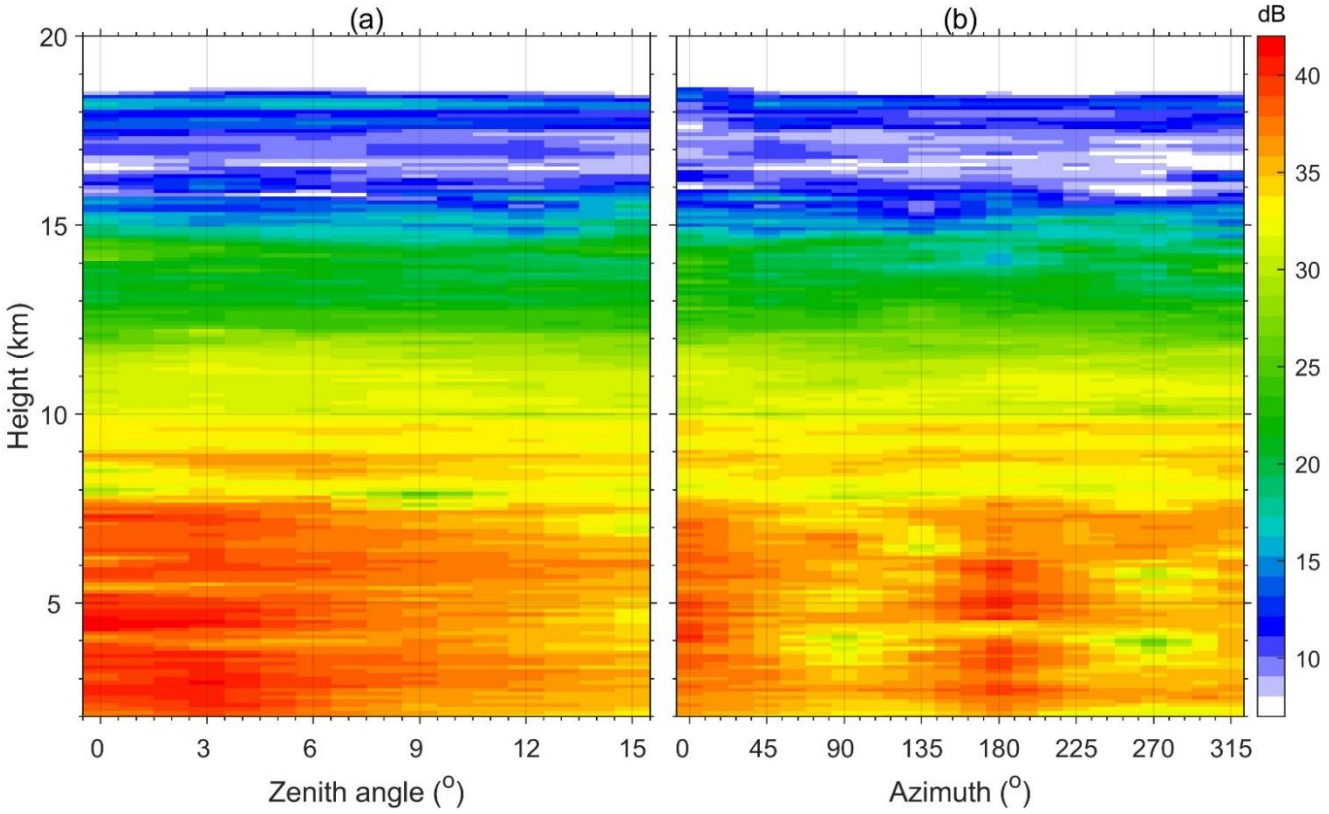

Figure 4. Daily mean height distribution of the signal-to-noise ratio (SNR, dB) versus zenith angle ((**a**) azimuth = 45°) and azimuth ((**b**) zenith angle = 12°) on 21 July 2021, in experiment #3.

To further evaluate the wind results derived from different zenith angles, we used the 41-beam data from 13:45 to 22:00 on 21 July 2021 in experiment #3 for analysis. We calculated the horizontal velocity at different zenith angles by two methods. The mean height profiles of zonal and meridional wind are shown in Figure 6, corresponding to five different zenith angles. The zonal winds for five different zenith angles showed little difference for the VAD method and GEO method below 15 km, while they were obviously different above 15 km. This indicates that turbulent motion is not uniform, and the anisotropy of turbulent motion is not negligible above 15 km. Taking the VAD method as an example, the zonal wind velocities were 19.3 m/s, 15.5 m/s, 10.2 m/s, 6.4 m/s, and 3.3 m/s for zenith angles of 3°, 6°, 9°, 12°, and 15°, respectively, at 18.5 km. The meridional winds of the five different zenith angles determined by the VAD method were similar to those determined by the GEO method below 10 km. However, they were different above 10 km. Furthermore, the meridional wind velocities derived from the VAD method were 8.59 m/s, 6.49 m/s, 4.72 m/s, 3.74 m/s, and 2.20 m/s for zenith angles of 3°, 6°, 9°, 12°, and 15°, respectively, at 18.2 km. At heights of 10–15 km, the meridional wind measured at zenith angles of 15° and 3° was obviously different from that of the remaining three zenith angles. The meridional wind velocity measured at the zenith angle of 15° was much lower than that at the other three zenith angles, while it was much larger at the zenith angle of 3°. In the range of 15–20 km, the meridional wind velocities measured at the five different zenith angles had the greatest difference. The meridional wind velocities calculated by

the VAD method at the zenith angle of 3° and 15° reached a maximum of 10 m/s and 5 m/s, respectively, while the maxima derived from the GEO method were 11 m/s and 6 m/s, respectively.

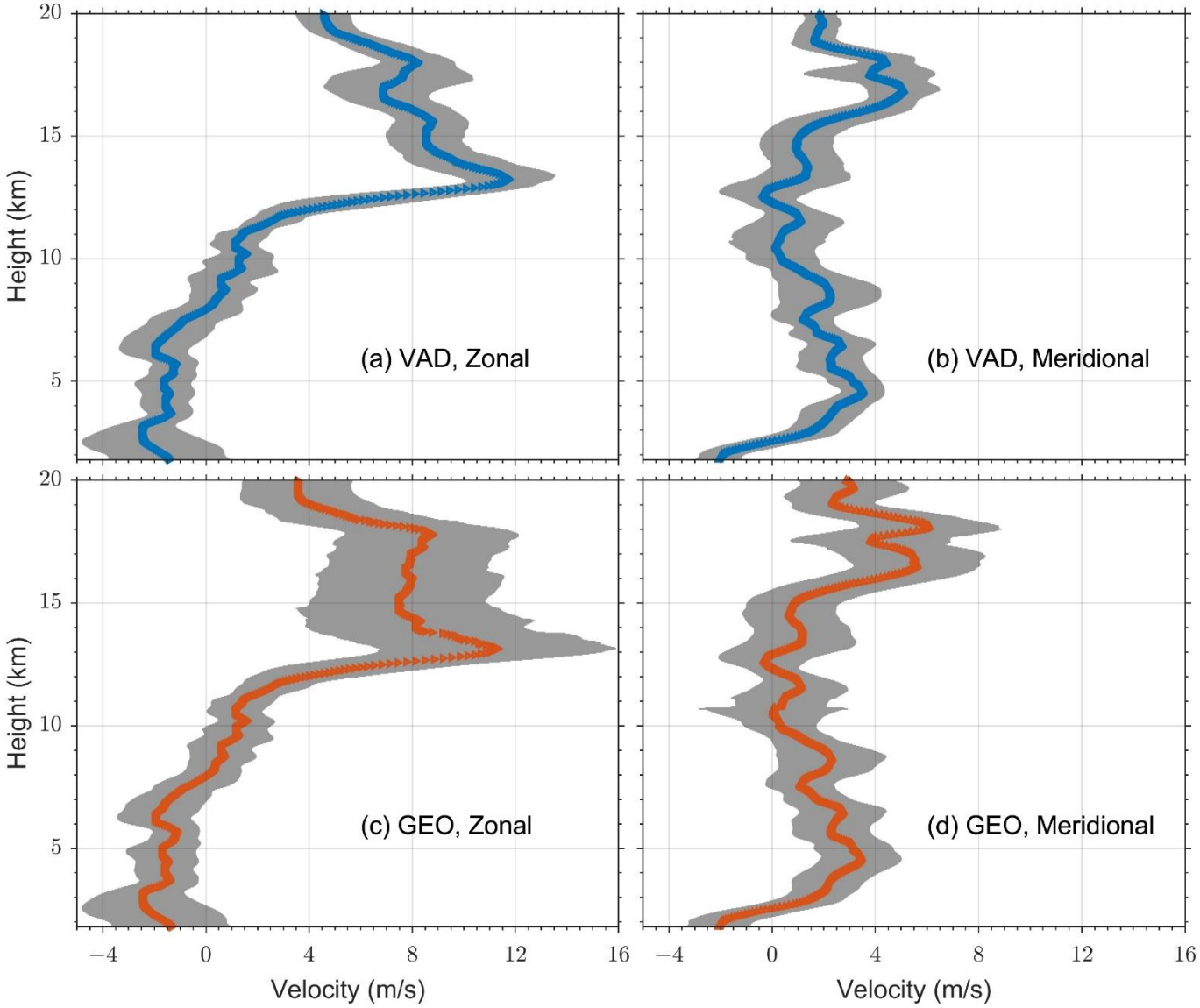

Figure 5. Daily mean height distribution of zonal wind (**a**,**c**) and meridional wind (**b**,**d**) derived by the VAD (**a**,**b**) and GEO (**c**,**d**) methods during 17–18 July 2021, in experiment #2. The shaded area represents 1-σ standard deviation.

SYISR-8 is located in Nanjing, while SYISR is located in Sanya [29]. There are only two radiosondes in Haikou and Xisha, which are more than 100 km away from Sanya. As a result, wind field of radiosondes in Haikou and Xisha have no reference significance. Therefore, we used the reanalysis data to analyze the accuracy of wind velocity obtained by SYISR. Figure 7 shows altitude variation for SYISR data by the VAD method and the GEO method and the reanalysis data of ERA5 [41] from 15:00 on 21 July 2021. For the VAD and GEO methods, 41-beam data had five different zenith angles. Here we chose the result of the zenith angle of 6° as an example. It is clear from Figure 7 that the altitude variation for SYISR data using the GEO and VAD methods and reanalysis data of ERA5 are similar. In order to analyze the statistical properties of the difference, we compared SYISR data and the reanalysis data of ERA5 from 13:45 to 22:00 on 21 July 2021, in experiment #3. We calculated average deviation (assuming the reanalysis data ERA5 were true values) and

corresponding standard deviation of the difference (SYISR data minus the reanalysis data of ERA5) and plotted this in Figure 8. Here we used the SYISR result of the VAD method as an example. It can be seen from Figure 8 that the average deviation varied with altitude, and the average deviation remained within plus or minus 2 m/s at all altitudes. In addition, we can find that the standard deviations of the difference for zonal wind and meridional wind were 1.1 m/s and 0.78 m/s, respectively. These results indicate a good consistency despite the different principles of wind measurement in SYISR and the reanalysis data of ERA5. Therefore, the SYISR could be used for tropospheric wind observation with reliable accuracy, which further proves the radar function expansion and capability verification for SYISR.

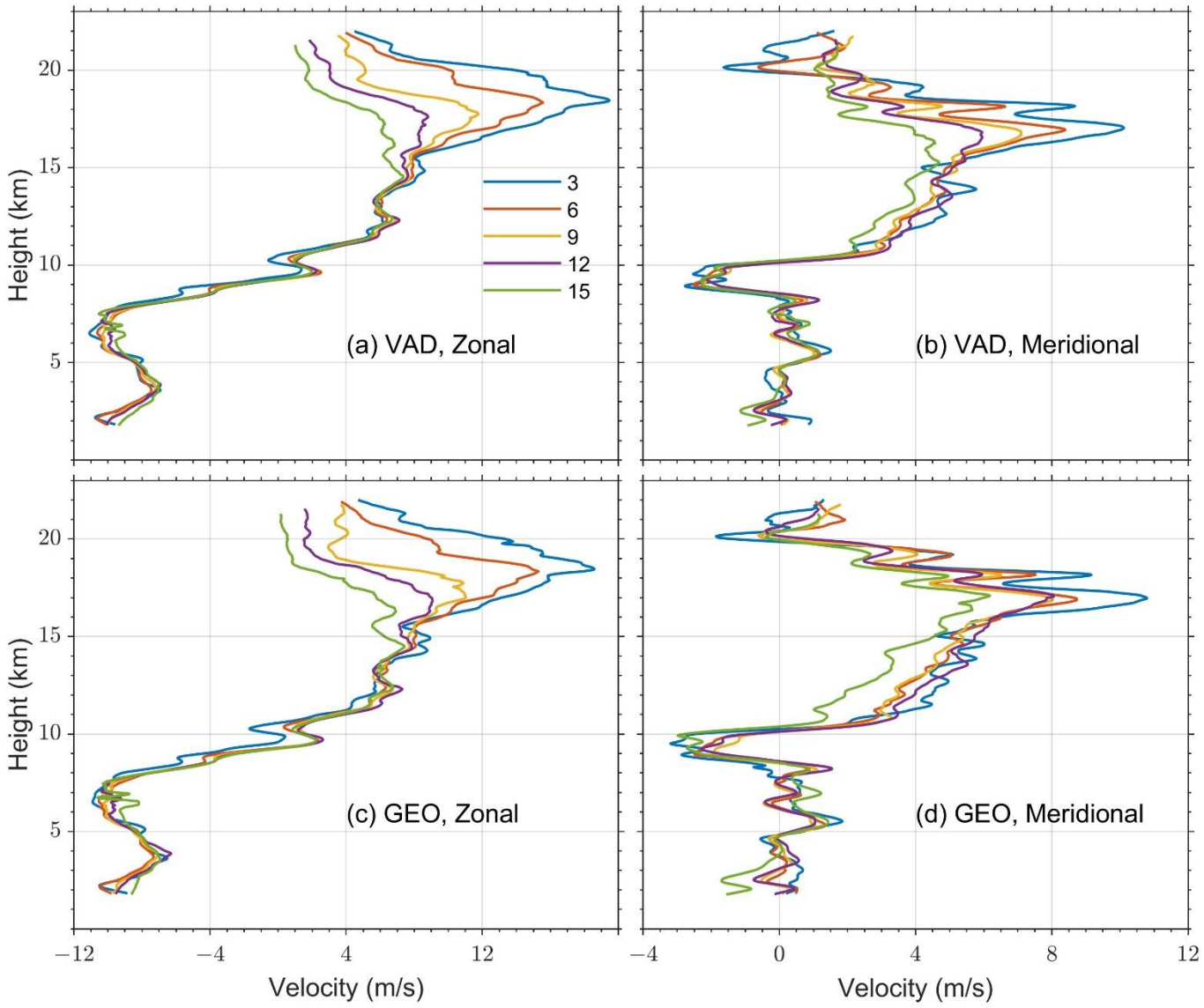

Figure 6. Daily mean height distributions of zonal wind (**a**,**c**) and meridional wind (**b**,**d**) derived from the VAD (**a**,**b**) and GEO (**c**,**d**) methods for different zenith angles from 3° to 15° with increments of 3° (distinguished by colors) on 21 July 2021, in experiment #3.

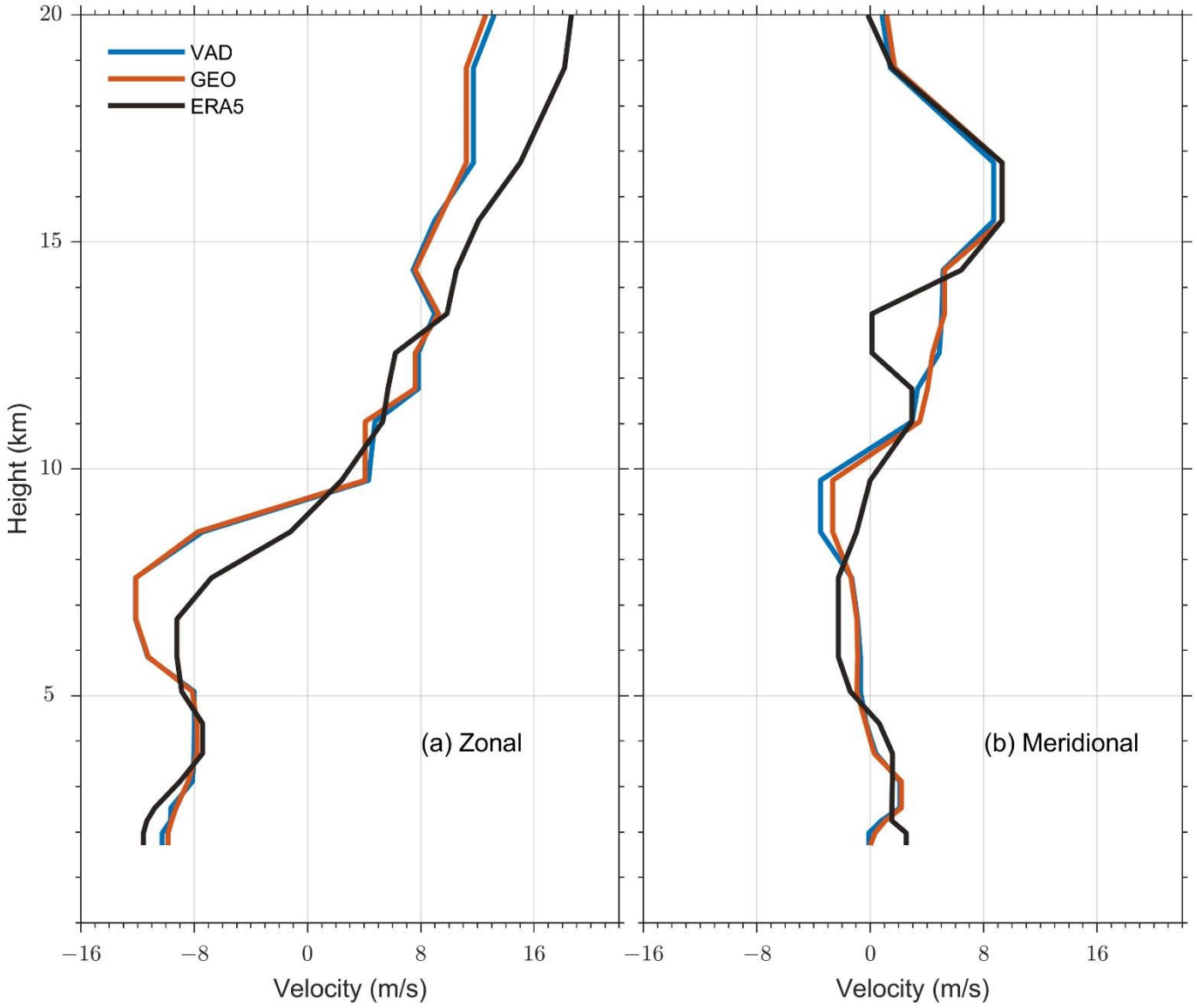

Figure 7. Height distributions of zonal wind (**a**) and meridional wind (**b**) derived from the VAD and GEO methods for zenith angles 6°, and the reanalysis ERA5 data (distinguished by colors) from 15:00 on 21 July 2021, in experiment #3.

3.3. Observation Results

We used the data from 9:00 on 17 July 2021 to 9:00 on 18 July in experiment #1 to analyze the variation in the radial velocity. In the 24 h observation experiment, rain occurred at approximately 15:00 on 17 July. Figure 9 shows the 24 h radial velocity measured with the west beam and south beam. According to Figure 9, the west beam and south beam detected a relatively large velocity of 6 m/s at approximately 15:00 because of the occurrence of rainfall. According to Figure 9a, there was an area where the radial velocity increased before rainfall at 10–20 km. The radial velocity appeared to be a large positive value before rainfall due to the large downward movement in this area. This may have been because the water vapor in the atmosphere was supersaturated and formed cloud droplets, which continued to accumulate and began to move downward, eventually forming rain. The westward velocity had a small positive value around 0–2 m/s at 5–10 km and a large negative value around 2–6 m/s at 12–20 km. The speed in the south direction reversed before and after rainfall in the range of 8–15 km. Before rainfall, the speed was positive,

and after rainfall, the speed was negative. The speed in the south direction was a small negative velocity except when the rain blew 8 km.

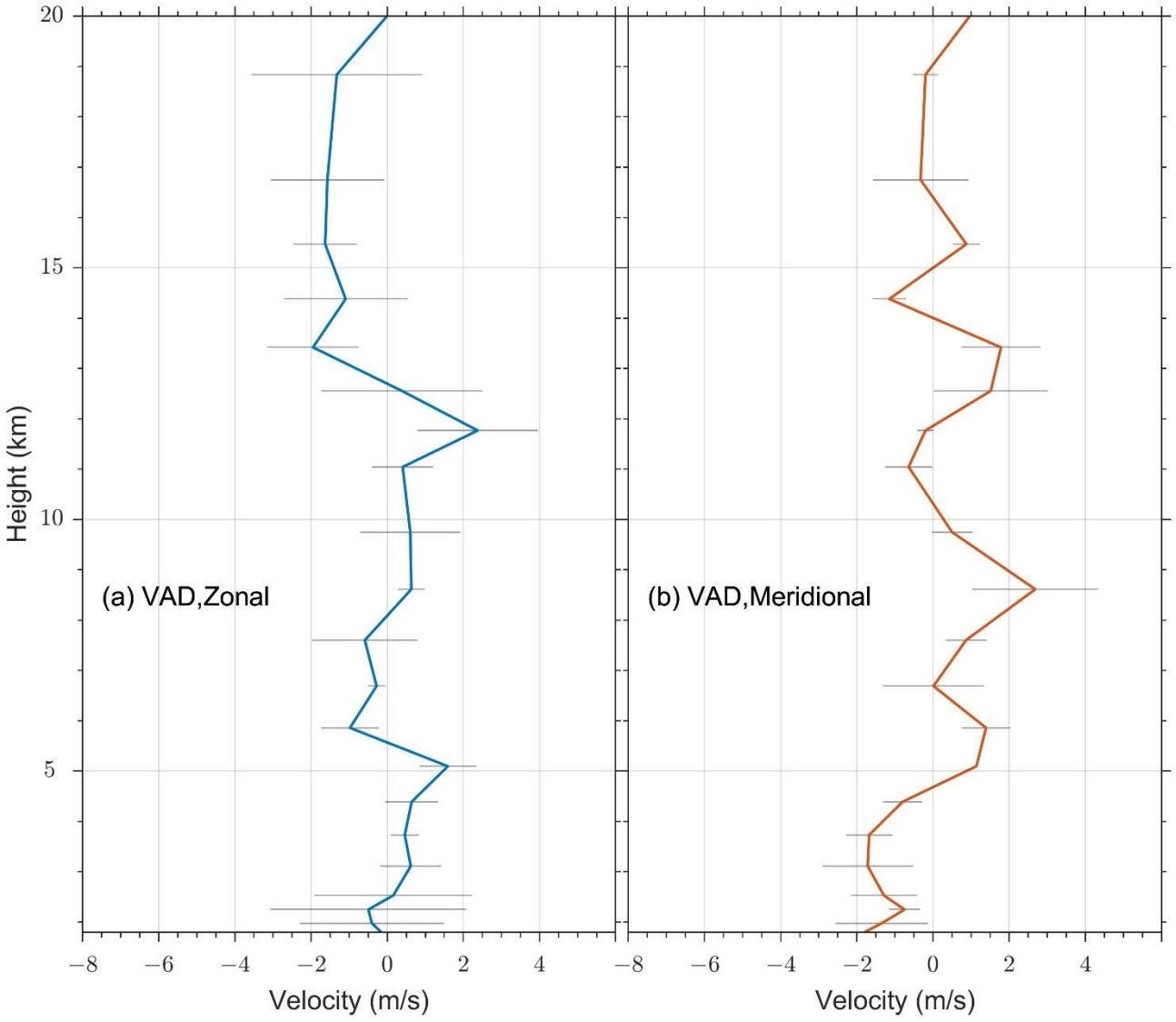

Figure 8. Daily height distribution of zonal wind average deviation (**a**) and meridional wind average deviation (**b**) derived by the VAD methods for zenith angle 6° on 21 July 2021, in experiment #3. Error bars represent 1–σ standard deviation.

Figure 10 shows wind barbs from 18:30 on 18 July 2021 to 9:00 on 19 July 2021, in experiment #2. The troposphere concentrates most of the water vapor, and it is the main area of atmospheric activity. Because troposphere gas is cold at the top and hot at the bottom, the troposphere presents significant characteristics such as strong vertical mixing of the atmosphere and uneven distribution of meteorological elements. Therefore, from the wind barbs, the atmospheric activity was strong below 13 km, and the horizontal wind velocity and direction changed rapidly. Within the height range of 13–20 km, the changes in horizontal wind velocity and wind direction were relatively small.

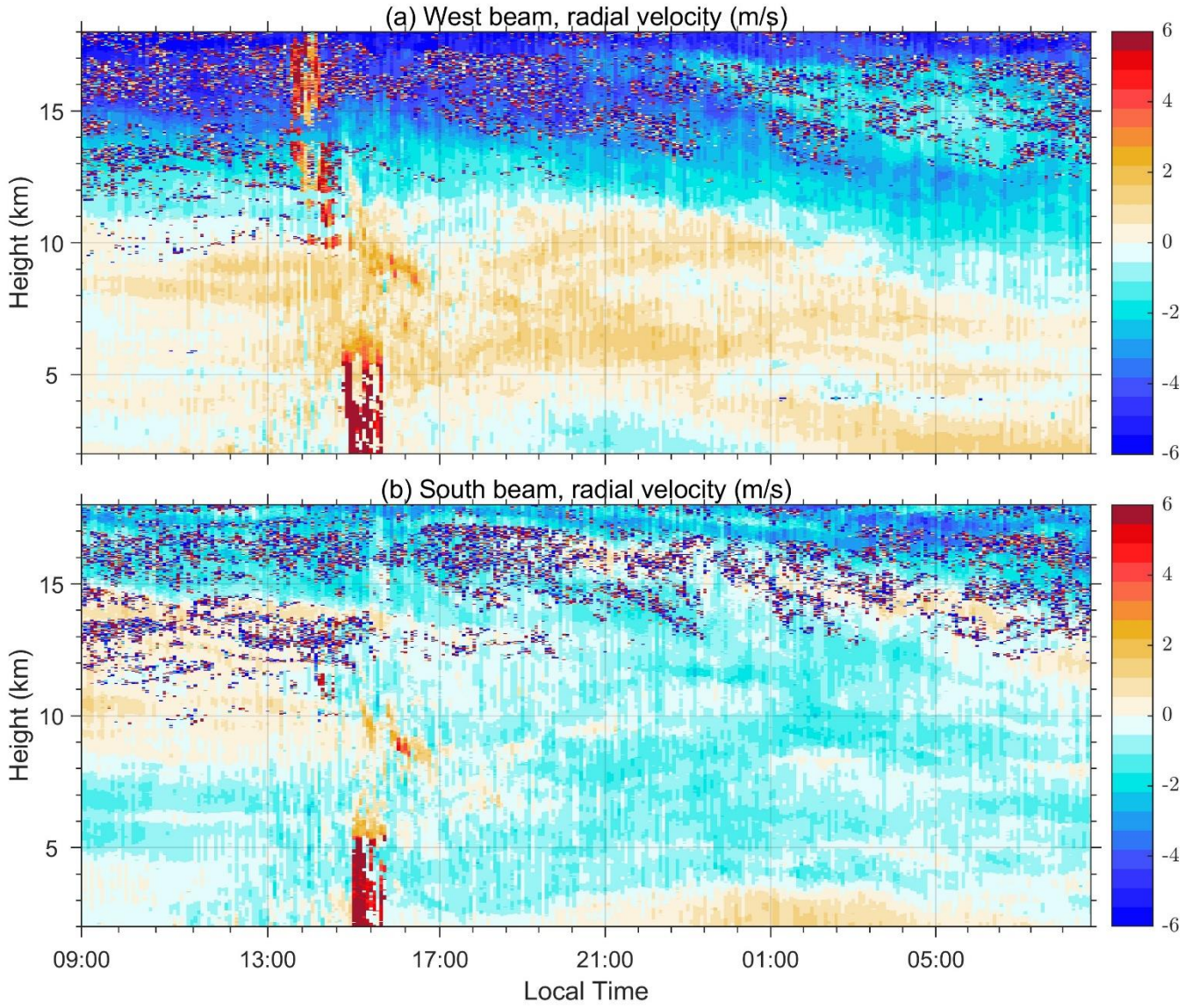

Figure 9. Radial velocity (m/s) for the west beam (**a**) and south beam (**b**) from 09:00 on 17 July 2021 to 09:00 on 18 July 2021, in experiment #1. The unit is m/s.

In the case of rainfall, the echo intensity of the rainfall is much stronger than that of the turbulent motion. It is therefore difficult to observe effective atmospheric turbulent echoes in rainfall environments [20]. As a result, it is necessary to distinguish the rain and turbulent echoes from the echo spectrum. In our experimental interval, we occasionally encountered a rainfall event at 15:00 on 17 July 2021, the spectrum of which is shown in Figure 11. According to the echo power spectrum of 8 azimuths in the rainfall environment, the Doppler shift of the rainfall was much higher than that of the atmospheric turbulent echo. Below 6 km, the velocity of turbulence was relatively low, the velocity of rainfall was relatively high, and the Doppler frequency shift of the two echoes was distinguishable. Another obvious feature was that the spectral width of the rainfall particles was much larger than that of the atmospheric turbulence. Rain always falls downward, so the rain echo always appears to the right of the atmospheric echo when the positive direction is approaching radar. Therefore, rain echoes and turbulent echoes can be clearly distinguished. From Figure 11, the atmospheric turbulence echo corresponding to the symmetrical beam showed good symmetry below 6 km. From the radial velocities in 8 azimuths, every azimuth had a positive Doppler frequency shift at 9–12 km, indicating that there was downward movement when rainfall occurred.

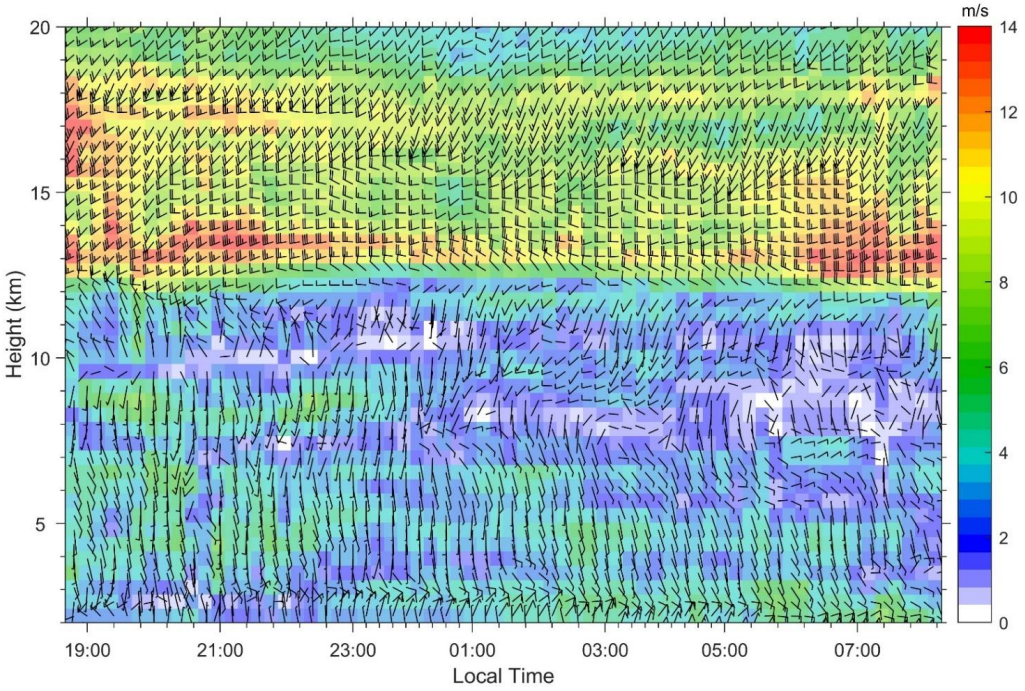

Figure 10. Wind barbs with respect to the local time and height from 19:00 on 18 July 2021 to 09:00 on 19 July 2021, in experiment #2. In addition to the shape of the array, the background color also represents the amplitudes of the wind. The unit is m/s.

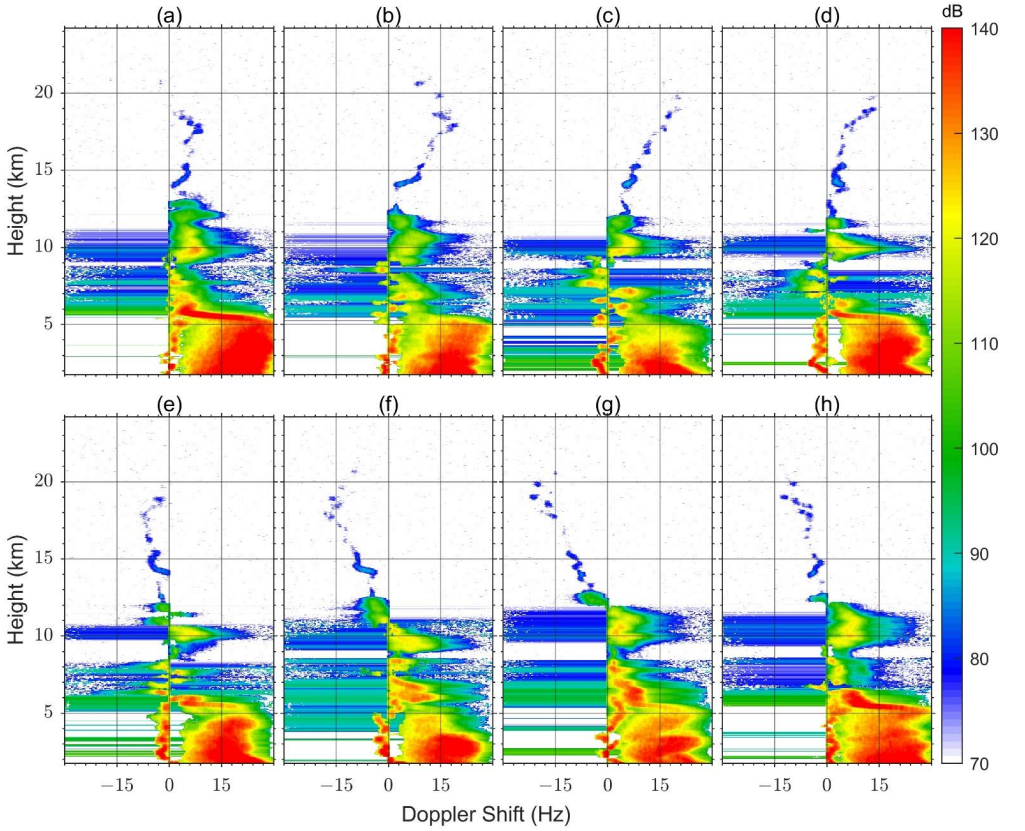

Figure 11. Echo power spectrum during rainfall corresponding to the eight azimuths of 0° ((**a**) north), 45° ((**b**) northeast), 90° ((**c**) east), 135° ((**d**) southeast), 180° ((**e**) south), 225° ((**f**) southwest), 270° ((**g**) west), and 315° ((**h**) northwest) with a zenith angle of 15°. The unit is dB, and the experiment time is 15:00 local time on 17 July 2021.

4. Conclusions

Based on the newly built Sanya Incoherent Scatter Radar (SYISR), we implemented three different multiple-beam experiments with 9, 25, and 41 beams to profile tropospheric wind during 17–21 July 2021. The radial velocity of each beam was derived from the Doppler spectra after a series of preprocessing steps and FFT algorithms. The horizontal velocities were then estimated using both GEO and VAD methods under different assumptions. The main conclusions are summarized as follows:

(1) In July, SYISR could obtain an effective echo of atmospheric turbulence up to 20 km. The measured SNR was determined by the intensity of the turbulence and controlled by the radar gain and beam width depending on the azimuth and elevation.
(2) Generally, both the GEO and VAD methods gave similar wind profiles. With increasing height, the discrepancy between the two methods gradually became nonnegligible. This indicates that the anisotropy of turbulence becomes significant at higher altitudes; therefore, the linear variation rather than the constant wind assumption works better. For the same methods, the discrepancy at higher altitudes among wind velocities derived from different zenith angle measurements was nonnegligible.
(3) By comparing the SYISR data with the reanalysis data of ERA5, the horizontal wind obtained by SYISR was in good agreement with the reanalysis data of ERA5, proving that SYISR can be used for tropospheric wind detection.
(4) During rainfall, we can distinguish the spectrum of rainfall and atmospheric turbulence from the power spectrum according to the spectral widths and Doppler frequency shifts.

Author Contributions: Conceptualization, N.Z. and X.Y.; methodology, N.Z. and X.Y.; software, N.Z.; validation, N.Z. and X.Y.; formal analysis, X.Y.; investigation, N.Z.; resources, N.Z., X.Y., J.W., Y.W. and Y.C.; data curation, N.Z., Y.W., Y.C., J.W., M.L. and J.L.; writing—original draft preparation, N.Z.; writing—review and editing, X.Y., F.D. and B.N.; visualization, N.Z. and X.Y.; supervision, X.Y.; project administration, X.Y.; funding acquisition, X.Y., F.D. and B.N. All authors have read and agreed to the published version of the manuscript.

Funding: This work was supported by the Project of Stable Support for Youth Team in Basic Research Field, CAS (YSBR-018), the Meridian Project and the National Natural Science Foundation of China (41427901).

Data Availability Statement: The reanalysis of ERA5 data used in the Figures 7 and 8 can be downloaded: (available online: https://cds.climate.copernicus.eu/cdsapp#!/dataset/reanalysis-era5-pressure-levels?tab=form (accessed on 20 May 2022)).

Conflicts of Interest: The authors declare no conflict of interest.

References

1. Wallace, J.M.; Hobbs, P.V. *Atmospheric Science*, 2nd ed.; University of Washington: Washington, DC, USA, 2006; ISBN 0-12-732951-X.
2. Ramaswamy, V.; Schwarzkopf, M.D.; Shine, K.P. Radiative forcing of climate from halocarbon-induced global stratospheric ozone loss. *Nature* **1992**, *355*, 810–812. [CrossRef]
3. Colwell, R.C.; Friend, A.W. The D Region of the Ionosphere. *Nature* **1936**, *137*, 782. [CrossRef]
4. Watt, R.A.; Bainbridge-Bell, L.H.; Wilkins, A.F.; Bowen, E.G. Return of radio waves from the middle atmosphere. *Nature* **1936**, *137*, 866. [CrossRef]
5. Gage, K.S.; Balsley, B.B. On the scattering and reflection mechanisms contributing to clear air radar echoes from the troposphere, stratosphere, and mesosphere. *Radio Sci.* **1980**, *15*, 243–257. [CrossRef]
6. Flock, W.L.; Balsley, B.B. VHF radar returns from the D region of the equatorial ionosphere. *J. Geophys. Res.* **1967**, *72*, 5537. [CrossRef]
7. May, P.T.; Strauch, R.G.; Moran, K.P.; Ecklund, W.L. Temperature sounding by RASS with wind profiler radars: A preliminary study. *IEEE Trans. Geosci. Remote Sens.* **1990**, *28*, 19–28. [CrossRef]
8. Zhou, C.; Qing, H.; Chen, G.; Gu, X.; Ni, B.; Yang, G.; Zhang, Y.; Zhao, Z. Wuhan Atmospheric Radio Exploration (WARE) radar: Implementation and initial results. *Atmos. Meas. Tech.* **2014**, *7*, 11901–11925. [CrossRef]
9. Harper, R.M.; Woodman, R.F. Preliminary multiheight radar observations of waves and winds in the mesosphere over Jicamarca. *J. Atmos. Terr. Phys.* **1977**, *39*, 959–963. [CrossRef]

10. Rastogi, P.K.; Bowhill, S.A. Scattering of radio waves from the mesosphere-2. evidence for intermittent mesospheric turbulence. *J. Atmos. Terr. Phys.* **1976**, *38*, 449–462. [CrossRef]
11. Rastogi, P.K.; Woodman, R.F. Mesospheric studies using the Jicamarca incoherent-scatter radar. *J. Atmos. Terr. Phys.* **1974**, *36*, 1217–1231. [CrossRef]
12. Woodman, R.F.; Guillen, A. Radar Observations of Winds and Turbulence in the Stratosphere and Mesosphere. *J. Atmos. Sci.* **1974**, *31*, 493–505. [CrossRef]
13. Fukao, S.; Kato, S.; Yokoi, S.; Harper, R.M.; Woodman, R.F.; Gordon, W.E. One full-day radar measurement of lower stratospheric winds over Jicamarca. *J. Atmos. Terr. Phys.* **1978**, *40*, 1331–1337. [CrossRef]
14. Fukao, S.; Kato, S.; Aso, T.; Sasada, M.; Makihira, T. Middle and upper atmosphere radar (MUR) under design in Japan. *Radio Sci.* **1980**, *15*, 225–231. [CrossRef]
15. Kato, S.; Ogawa, T.; Tsuda, T.; Sato, T.; Kimura, I.; Fukao, S. The middle and upper atmosphere radar: First results using a partial system. *Radio Sci.* **1984**, *19*, 1475–1484. [CrossRef]
16. Riggin, D.M.; Liu, H.L.; Lieberman, R.S.; Roble, R.G.; Russell, J.M., III; Mertens, C.J.; Mlynczak, M.G.; Pancheva, D.; Franke, S.J.; Murayama, Y.; et al. Observations of the 5-day wave in the mesosphere and lower thermosphere. *J. Atmos. Terr. Phys.* **2006**, *68*, 323–339. [CrossRef]
17. Larsen, M.F.; Rutger, J.; Holden, D.N. Direct Measurements of Vertical-Velocity Power Spectra with the Sousy-VHF-Radar Wind Profiler System. *J. Atmos. Sci.* **1987**, *44*, 3442–3448. [CrossRef]
18. Chen, G.; Cui, X.; Chen, F.; Zhao, Z.; Wang, Y.; Yao, Q.; Wang, C.; Lü, D.; Zhang, S.; Zhang, X.; et al. MST radars of Chinese meridian project: System description and atmospheric wind measurement. *IEEE Trans. Geosci. Remote Sens.* **2016**, *54*, 4513–4523. [CrossRef]
19. Qing, H.; Zhou, C.; Zhao, Z.; Chen, G.; Ni, B.; Gu, X.; Yang, G.; Zhang, Y. A statistical study of inertia gravity waves in the troposphere based on the measurements of Wuhan Atmosphere Radio Exploration (WARE) radar. *J. Geophys. Res. Atmos.* **2014**, *119*, 3701–3714. [CrossRef]
20. Qing, H.; Zhou, C.; Zhao, Z.; Ni, B.; Zhang, Y. Inertia gravity wave activity in the troposphere and lower stratosphere observed by Wuhan MST radar. *Sci. China Earth Sci.* **2016**, *59*, 1066–1073. [CrossRef]
21. Tian, Y.F.; Lü, D.R. Comparison of Beijing MST radar and radiosonde horizontal wind measurements. *Adv. Atmos. Sci.* **2017**, *34*, 39–53. [CrossRef]
22. Fukao, S.; Sato, T.; Yamasaki, N.; Kato, S. Winds measured by a UHF Doppler radar and rawinsondes: Comparisons made on twenty-six days (August-september 1977) at Arecibo, Puerto Rico. *J. Appl. Meteor.* **1982**, *21*, 1357–1363. [CrossRef]
23. Ierkic, H.M.; Woodman, R.F.; Perillat, P. Ultrahigh vertical resolution radar measurements in the lower stratosphere at Arecibo. *Radio Sci.* **1990**, *25*, 941–952. [CrossRef]
24. Röttger, J.; Czechowsky, P.; Schmidt, G. First low-power VHF radar observation of tropospheric, stratospheric and mesospheric winds and turbulence at the Arecibo Observatory. *J. Atmos. Terr. Phys.* **1981**, *43*, 789–800. [CrossRef]
25. Sato, T.; Woodman, R.F. Fine Altitude resolution observations of stratospheric turbulent layers by the Arecibo 430 MHZ radar. *J. Atmos. Sci.* **1982**, *39*, 2546–2552. [CrossRef]
26. Sato, T.; Woodman, R.F. Fine Altitude Resolution Radar Observations of Upper-Tropospheric and Lower-Stratospheric Winds and Waves. *J. Atmos. Sci.* **1982**, *39*, 2539–2545. [CrossRef]
27. Woodman, R.F. High-altitude resolution stratospheric measurements with the Arecibo 430Mhz radar. *Radio Sci.* **1980**, *15*, 417–422. [CrossRef]
28. Yue, X.; Wan, W.; Ning, B.; Jin, L. An active phased array radar in China. *Nat. Astron.* **2022**, *6*, 619. [CrossRef]
29. Yue, X.; Wan, W.; Xiao, H.; Zeng, L.; Ke, C.; Ning, B.; Ding, F.; Zhao, B.; Jin, L.; Li, C.; et al. Preliminary experimental results by the prototype of Sanya Incoherent Scatter Radar. *Earth Planet. Phys.* **2020**, *4*, 579–587. [CrossRef]
30. Hildebrand, P.H.; Sekhon, R.S. Objective Determination of the Noise Level in Doppler Spectra. *J. Appl. Meteor.* **1974**, *13*, 808–811. [CrossRef]
31. May, P.T.; Strauch, R.G. An Examination of Wind Profiler Signal Processing Algorithms. *J. Atmos. Ocean. Technol.* **1989**, *6*, 731–735. [CrossRef]
32. Strauch, R.G.; Merritt, D.A.; Moran, K.P.; Earnshaw, K.B.; Kamp, D.V.D. The Colorado Wind-Profiling Network. *J. Atmos. Ocean. Technol.* **1984**, *1*, 37–49. [CrossRef]
33. Strauch, R.G.; Weber, B.L.; Frisch, A.S.; Little, C.G.; Merritt, D.A.; Moran, K.P.; Welsh, D.C. The Precision and Relative Accuracy of Profiler Wind Measurements. *J. Atmos. Ocean. Technol.* **1987**, *4*, 563–571. [CrossRef]
34. Hogg, D.C.; Decker, M.T.; Guiraud, F.O.; Earnshaw, K.B.; Merritt, D.A.; Moran, K.P.; Sweezy, W.B.; Strauch, R.G.; Westwater, E.R.; Little, C.G. An Automatic Profiler of the Temperature, Wind and Humidity in the Troposphere. *J. Appl. Meteor.* **1983**, *22*, 807–831. [CrossRef]
35. Browning, K.A.; Wexler, R. The Determination of Kinematic Properties of a Wind Field Using Doppler Radar. *J. Appl. Meteor.* **1968**, *7*, 105–113. [CrossRef]
36. Matejka, T.; Srivastava, R.C. An Improved Version of the Extended Velocity-Azimuth Display Analysis of Single-Doppler Radar Data. *J. Atmos. Ocean. Technol.* **1991**, *8*, 453–466. [CrossRef]
37. Wang, Y.; Wei, M.; Shi, Q. First Spaceborne Version of Velocity-Azimuth Display Technique for Wind Field Retrieval on Cloud and Precipitation Radar. *Atmosphere* **2020**, *11*, 1089. [CrossRef]

38. Waldteufel, P.; Corbin, H. On the Analysis of Single-Doppler Radar Data. *J. Appl. Meteorol. Clim.* **1979**, *18*, 532–542. [CrossRef]
39. Larsen, M.F.; Röttger, J. Observations of Thunderstorm Reflectivities and Doppler Velocities Measured at VHF and UHF. *J. Atmos. Ocean. Technol.* **1987**, *4*, 151–159. [CrossRef]
40. Gage, K.S.; Balsley, B.B. Doppler Radar Probing of the Clear Atmosphere. *Bull. Amer. Meteor. Soc.* **1978**, *59*, 1074–1094. [CrossRef]
41. Hersbach, H.; Bell, B.; Berrisford, P.; Biavati, G.; Horányi, A.; Sabater, J.M.; Nicolas, J.; Peubey, C.; Radu, R.; Rozum, I.; et al. ERA5 Hourly Data on Pressure Levels from 1979 to Present. Copernicus Climate Change Service (C3S) Climate Data Store (CDS). 2018. Available online: https://cds.climate.copernicus.eu/cdsapp#!/dataset/reanalysis-era5-pressure-levels?tab=form (accessed on 20 May 2022).